24. H. Imai, H. Yurimoto, *Lunar Planet. Sci.* **XXXII**, 1580 (abstract) (2001).
25. H. Hiyagon, A. Hashimoto, *Science* **283**, 828 (1999).
26. M. I. Petaev, J. A. Wood, *Meteorit. Planet. Sci.* **33**, 1123 (1998).
27. A. M. Davis, G. J. MacPherson, *Meteoritics* **29**, A458 (abstract) (1994).
28. A. Ruzicka, W. V. Boynton, *Meteorit. Planet. Sci.* **30**, 570 (abstract) (1995).
29. E. R. D. Scott, A. N. Krot, *Meteorit. Planet. Sci.* **36**, 1307 (2001).
30. J. A. Wood, *Earth Planet. Sci. Lett.* **56**, 32 (1981).
31. Some minerals within individual CV CAIs, such as melilite and anorthite, have ^{16}O-poor compositions relative to coexisting spinel and pyroxene. If this resulted from gas-solid exchange between the ^{16}O-poor gas and an initially ^{16}O-rich CAI, our results indicate that the exchange probably occurred after the formation of the Wark-Lovering and accretionary rims. An alternative model (*16*, *37*), in which CAIs exchanged with ^{16}O-poor nebular gas during partial remelting and recrystallization, requires a large transient excursion in the isotopic composition of gas in the CAI-forming region in between the time the CAIs formed and the time their Wark-Lovering and accretionary rims formed.
32. The petrologic observations indicating that CAIs were largely absent when Fe-Mg chondrules were melted include (i) absence of relic CAIs inside Fe-Mg chondrules or CAI chondrule compound objects, (ii) preservation of Wark-Lovering rims around most CAIs, and (iii) the slow inferred cooling rates during crystallization of igneous CAIs (1 to 10 K hour^{-1}) compared with those inferred for chondrules (100 to 1000 K hour^{-1}).
33. M. H. Thiemens, *Science* **283**, 341 (1999).
34. J. A. Wood, *Astrophys. J.* **503**, L101 (1998).
35. D. S. Ebel, L. Grossman, *Geochim. Cosmochim. Acta* **64**, 339 (2000).
36. H. Yurimoto, Y. Asada, K. Hirai, *Meteorit. Planet. Sci.* **36**, A230 (abstract) (2001).
37. H. Yurimoto, M. Ito, H. Nagasawa, *Science* **282**, 1874 (1998).
38. The supplementary data are available on *Science* Online at www.sciencemag.org/cgi/content/full/295/5557/1051/DC1.
39. This work was supported by NASA grants NAG5-10610 (A.N.K., P.I.), NAG5-4212 (K. Keil, P.I.), NAG5-4704 (K.D.M., P.I.), NAG5-10523 (L.A.L., PI), and NAG5-7396 and NAG5-10468 (G.J.M., P.I.). This is Hawaii Institute of Geophysics and Planetology publication 1145 and School of Ocean and Earth Science and Technology publication 5928.

16 November 2001; accepted 7 January 2002

The Mantle Flow Field Beneath Western North America

P. G. Silver[1]* and W. E. Holt[2]

Although motions at the surface of tectonic plates are well determined, the accompanying horizontal mantle flow is not. We have combined observations of surface deformation and upper mantle seismic anisotropy to estimate this flow field for western North America. We find that the mantle velocity is 5.5 ± 1.5 centimeters per year due east in a hot spot reference frame, nearly opposite to the direction of North American plate motion (west-southwest). The flow is only weakly coupled to the motion of the surface plate, producing a small drag force. This flow field is probably due to heterogeneity in mantle density associated with the former Farallon oceanic plate beneath North America.

It is surprising that after more than three decades into the plate tectonic revolution, we have so little direct observation of the mantle flow field that accompanies plate motion. The most straightforward measure of mantle flow is provided by the trajectory of subducted slabs whose seismicity and high seismic velocities provide tracers of the flow. Yet even in subduction zone environments there is evidence for complex three-dimensional flow both above and below the slab (*1*–*4*). Far from slabs, even less information is available to delineate the mantle flow field. Various approaches have been used to predict this flow field theoretically. One approach (*5, 6*) calculates the mantle flow field that would result if the motions of the plates are imposed as boundary conditions, in addition to considering the trenches and ridges as sources and sinks of mass. This flow field is dominated by plate-entrained flow and a corresponding counterflow. More recently, several groups have calculated the instantaneous field arising from density anomalies in the mantle inferred from either seismic tomography or the history of subduction (*7, 8*). The plates are again taken as boundary conditions on this flow field, and a plate velocity is chosen such that the integrated torque on each plate vanishes. Both approaches adequately predict plate velocities, although the accompanying mantle flow fields and driving forces are different. The major difference in these approaches has to do with the role of density anomalies that are not directly attached to currently subducting plates, but are either inferred from global seismic tomography or from the long-term history of subduction. One way of testing these models is to measure the flow field beneath a plate that is not attached to a slab, but that has a mantle density anomaly beneath it and therefore different mantle flow fields predicted by (*5, 6*) and (*7, 8*). The North American plate has these characteristics (*9*).

Here we provide such a test, using a new procedure for inferring mantle flow velocity beneath western North America through the simultaneous analysis of surface deformation data [from Global Positioning System (GPS) and Quaternary fault slip data] and mantle deformation inferred from seismic anisotropy. Westernmost North America is ideal in particular because there is little lithosphere beneath the crust (*10*–*12*). This means that the anisotropy is dominated by the differential horizontal motion between the lithosphere and underlying mantle, producing a deformation fabric in the asthenosphere (*13*), associated with simple shear (*14*). The magnitude and direction of horizontal shear within the asthenosphere depends on the vector difference, $\mathbf{V}_\phi$, between the horizontal velocity of the lithosphere, $\mathbf{V}_\ell$, and the horizontal component of velocity of the mantle, $\mathbf{V}_m$, at the base of the asthenosphere (*15*). Writing $\mathbf{V}_m(\hat{\mathbf{r}}) = r_a\omega_m \times \hat{\mathbf{r}}$, $\mathbf{V}_p(\hat{\mathbf{r}}) = r_e\omega_p \times \hat{\mathbf{r}}$, and $\mathbf{V}_\ell(\hat{\mathbf{r}}) = \mathbf{V}_p(\hat{\mathbf{r}}) + \mathbf{V}_t(\hat{\mathbf{r}})$, this vector difference can be expressed as

$$\mathbf{V}_\phi(\hat{\mathbf{r}}) = r_e\omega_p \times \hat{\mathbf{r}} + \mathbf{V}_t(\hat{\mathbf{r}}) - r_a\omega_m \times \hat{\mathbf{r}} \quad (1)$$

where r_e is Earth's radius, ω_p is the angular velocity for the stable portion of the plate, $\mathbf{V}_t(\hat{\mathbf{r}})$ is the lithosphere velocity relative to the stable portion of the plate [i.e., $\mathbf{V}_t(\hat{\mathbf{r}}) = 0$ for a rigid plate], ω_m is the angular velocity of the mantle at the base of the asthenosphere at radius r_a, and $\hat{\mathbf{r}}$ is Earth's position unit vector (*16*).

The orientation of $\mathbf{V}_\phi(\hat{\mathbf{r}})$ can be constrained from seismic anisotropy; for finite strains of order unity, the *a* axis of olivine tends to orient parallel to the flow line (*17*) and hence parallel to $\mathbf{V}_\phi(\hat{\mathbf{r}})$. For a vertically propagating shear wave recorded at a single station, the fast polarization direction, ϕ, of a split shear wave will be parallel to $\mathbf{V}_\phi(\hat{\mathbf{r}})$ as well (*14*). If we have an observation of ϕ, we can then express the orientation of $\mathbf{V}_\phi(\hat{\mathbf{r}})$ as $\hat{\mathbf{V}}_\phi(\hat{\mathbf{r}}) = \pm\hat{\mathbf{V}}_s(\hat{\mathbf{r}})$, where $\pm\hat{\mathbf{V}}_s(\hat{\mathbf{r}})$ denotes the orientation of ϕ subject to a 180° ambiguity. Within or across a plate boundary zone, where $\mathbf{V}_t(\hat{\mathbf{r}})$ changes as a function of $\hat{\mathbf{r}}$, the three components of ω_m in Eq. 1 can be uniquely determined with as few as three observations of ϕ (Fig. 1) (*18*).

We used splitting data from only the red areas of Fig. 2, where asthenospheric flow is likely to dominate the anisotropic contribution (*19*). For $\hat{\mathbf{V}}_s(\hat{\mathbf{r}})$ in this western region, we used data from a recent study (*20*) augmented by additional data in the region (*14, 21*) (Fig. 2). For $\mathbf{V}_t(\hat{\mathbf{r}})$, we used the interpolated surface velocity field (*22, 23*) derived from GPS observations (*24*–*33*) and Quaternary fault slip rates (*34, 35*).

[1]Department of Terrestrial Magnetism, Carnegie Institution of Washington, Washington, DC 20015, USA. [2]State University of New York, Stony Brook, NY 11794, USA.

*To whom correspondence should be addressed. E-mail: silver@dtm.ciw.edu

We first sought to determine whether the mantle leads or trails the hot spot motion of the plate (i.e., moving west-southwest or east-northeast with respect to the plate). A "leading" model is clearly inconsistent with the splitting data, yielding predictions that are nearly orthogonal to the observed values in California (Figs. 1 and 3A). Of the "trailing" models, we first consider the case in which the mantle is fixed in a hot spot frame, which predicts ω_p = 0.28° per million years (My) (*36*) and ω_m = 0°/My in Eq. 1. This "trailing" model is more successful, being broadly consistent with the observations (Fig. 3B). From this we can conclude that, to first order, the mantle trails the plate. The predicted splitting values, however, are systematically rotated counterclockwise with respect to the observations in the east, and clockwise for stations in the west (Fig. 3B). We next performed a formal inversion to estimate the three components of ω_p in the reference frame ω_m = 0°/My, where the mantle is assumed to be stationary. We find that ω_p = 1.3 ± 0.3°/My and rotates about a pole located at a latitude of −65° ± 4° and longitude of 49° ± 1° (1σ error) (*37*). This model (Fig. 3C) is close to the hot spot pole (*38*), although the angular velocity is much higher than what would be predicted if the mantle were indeed stationary in a hot spot frame. In the hot spot frame, the mantle moves about a pole ω_m = (+63°, −122°, 1.1°/My), which yields easterly mantle velocities of about 5.5 ± 1.5 cm/year (1σ error) beneath western North America (Fig. 4). Because the uncertainties in the hot spot frame (*36*) are included within the formal uncertainties in ω_m, these velocities are significantly different from zero in a hot spot frame (*39*). The entire data set therefore requires a nonzero component of eastward flow in the mantle beneath westernmost North America (*40*).

One might argue that the anisotropy directions in the southern part of the model are due to local effects, such as a mantle keel beneath the western Transverse Ranges (*41*). This is unlikely, however, because observations over a large area—on the Pacific Plate to the west, in Baja, California, to the south, and in the Basin and Range to the east—also require eastward flow. Fossil fabric within the lithospheric mantle is also an unlikely explanation, because the tomography argues for relatively thin mantle lithosphere throughout this region (*10*). It is of course possible to find a more complex mantle flow field than the uniform field assumed here, which might provide a better match to the observations and possibly a lower magnitude of mantle flow velocity. If, however, the mantle flow field beneath westernmost North America is a long-wavelength feature, then nonzero eastward mantle velocities provide the simplest and best fitting solution.

This study represents a direct measurement of mantle flow velocity in a region other than a subducted slab, and it can be used to test model predictions of this flow field. Clearly these data are inconsistent with a mantle that leads the plate, is moving coherently with the stable part of North America (*42*), or is stationary in a hot spot frame. The inferred mantle velocity field is also inconsistent with flow models driven by the surface motions of the plates that include shallow return flow, because these models predict southward flow beneath western North America (*5, 6*). One flow

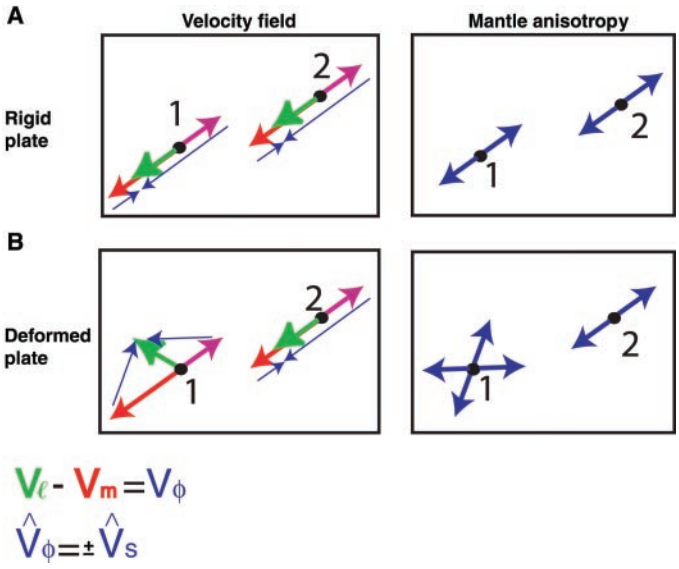

Fig. 1. Extracting the velocity of an overlying plate with respect to the mantle for a deforming plate. Map views in hot spot frame are shown for rigid plate (**A**) and deformed plate (**B**) velocity fields (left) and corresponding anisotropy directions for $\pm\hat{\mathbf{V}}_s$ (right) for locations 1 and 2 on the plate. Arrows give lithosphere velocity $\mathbf{V}_\ell$ (green), mantle velocity $\mathbf{V}_m$ (two cases: red for mantle leading plate case, violet for mantle trailing plate case), and differential velocity vector $\mathbf{V}_\phi = \mathbf{V}_\ell - \mathbf{V}_m$ (blue vector). For a rigid plate, $\pm\hat{\mathbf{V}}_s$ is the same for both leading and trailing cases. For a deformed plate, however, values of $\pm\hat{\mathbf{V}}_s$ are completely different. For example, in (B), if $\mathbf{V}_m$ leads the plate (red arrow), then $\mathbf{V}_\phi$ is oriented in an almost northerly direction at location 1, and hence $\pm\hat{\mathbf{V}}_s$ is oriented north-northeast–south-southwest. If $\mathbf{V}_m$ trails the plate (violet arrow), then $\hat{\mathbf{V}}_\phi(\hat{\mathbf{r}})$ and $\pm\hat{\mathbf{V}}_s$ are oriented westerly and east-west, respectively.

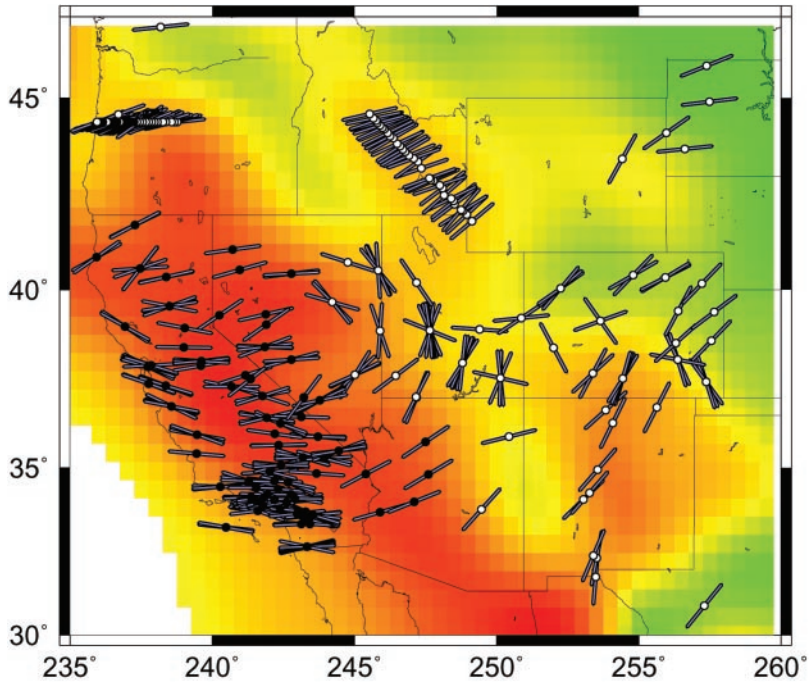

Fig. 2. Map of available splitting observations (*14, 20, 21*) superimposed on mantle shear velocity at a depth of 150 km (*10*). Circles give station locations. Bar orientations give splitting fast polarization direction ϕ, which equals ± $\hat{V}_s$. We use data only from "red" (slow) areas (solid circles), where the influence of lithosphere on anisotropy is expected to be small.

model that gives roughly the correct direction is the instantaneous flow driven by density anomalies in the mantle that are inferred from the history of subduction during the last 200 My (*7, 8*). In this model, the sinking Farallon slab beneath mid–North America entrains flow toward the center of the plate. In western North America this flow is approximately northeast (*43, 44*), which is compatible with our results. Our observations thus suggest that at the base of the asthenosphere there is east-directed flow beneath western North America that is produced by the sinking Farallon slab. Detailed information about the Farallon slab has been obtained by seismic tomography (*9*) where high-velocity anomalies in the mantle are associated with various fragments of the Farallon slab. Some of the fragments apparently have sinking velocities greater than 2 cm/year averaged over the last 16 My. If this sinking velocity can be translated to a horizontal velocity, it would make that velocity approximately compatible with the lower bound on the 95% confidence region of our velocity estimate.

Our results have implications for the nature of the flow field that accompanies plate tectonics. First, at least for this region of western North America, the mantle does not constitute a driving force for the plate, but rather a drag force. Yet this drag force must be very weak. Plate deformation in the western United States is modeled remarkably well by boundary stresses and stresses produced by gravitational potential energy differences (*35, 45–47*), with no discernible contribution from basal shear. The high strain rates within the asthenosphere implied by this flow field consequently require very low viscosities in order to produce small basal tractions. Recent viscosity estimates for the crust and upper mantle in this tectonic environment confirm this (*48*). Thus, there is a well-developed asthenospheric decoupling zone beneath western North America. A consequence of this decoupling is that, as we have found, a significant component of

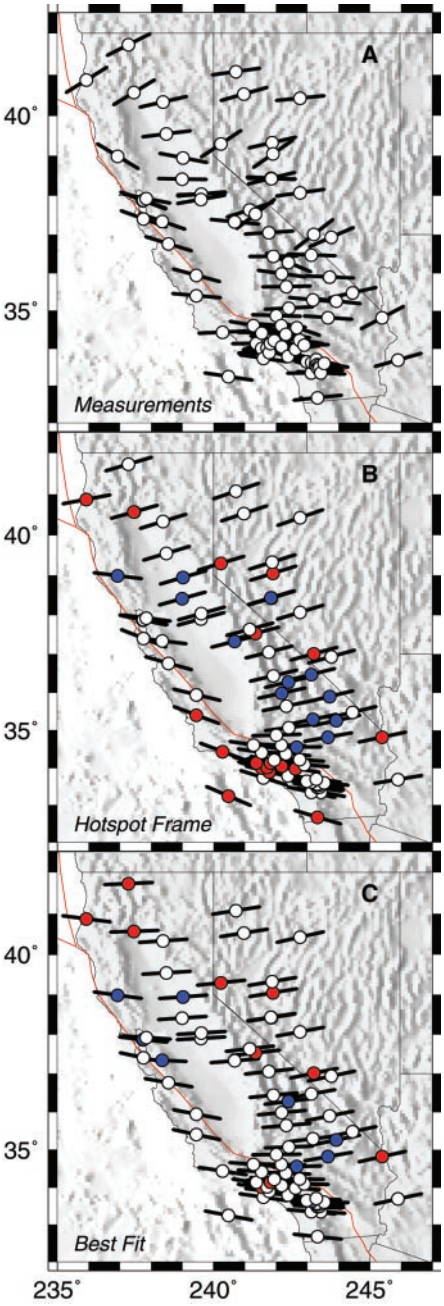

Fig. 3. (**A**) Shear-wave splitting data set [$\pm\hat{\mathbf{V}}_s(\hat{\mathbf{r}})$, only station means shown; see text], with predicted values from two models: mantle stationary in a hot spot frame (**B**) and formal inversion for mantle velocity (**C**). In (B) and (C), misfit angle is color-coded as follows: Red, model is clockwise by more than 14° with respect to data; blue, model is counterclockwise by more than 14° with respect to data; white, neither threshold is reached. Note that the hot spot model is broadly consistent with observations but exhibits a systematic misfit pattern that is substantially reduced by the results of the formal inversion (C).

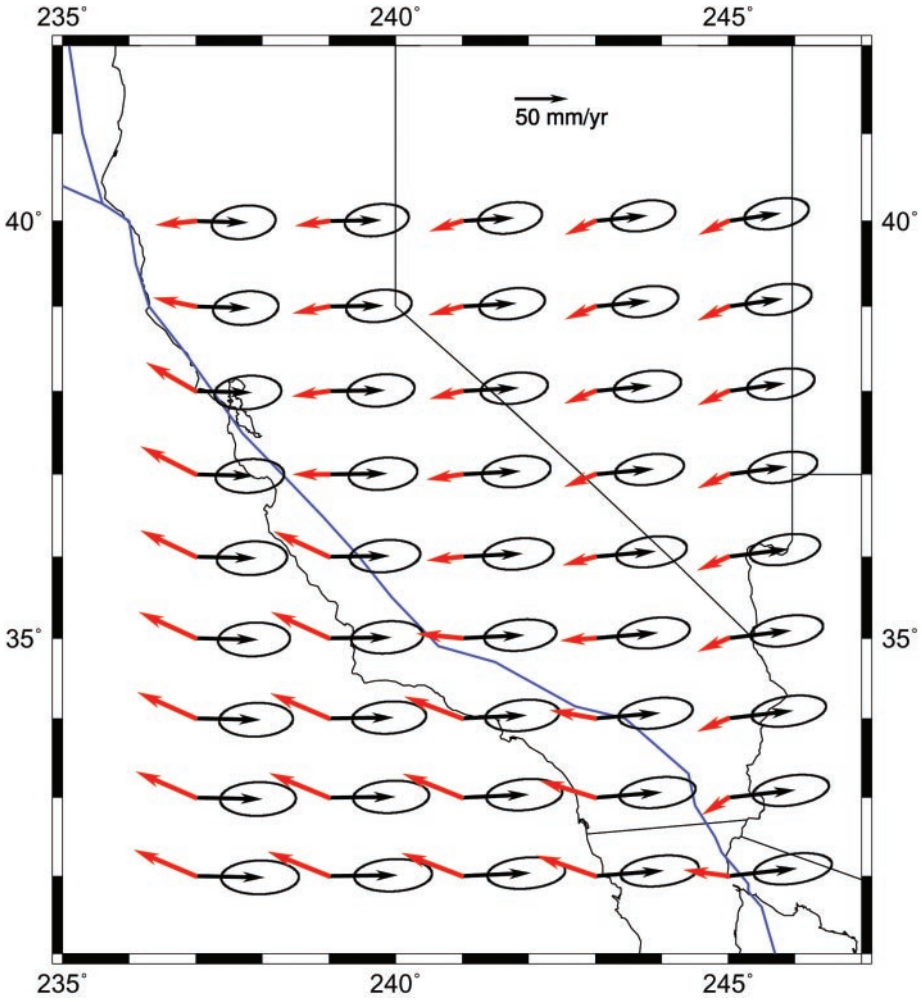

Fig. 4. Estimated mantle velocity, $\mathbf{V}_m(\hat{\mathbf{r}})$, in a hot spot frame (black arrows) along with lithosphere motion, $\mathbf{V}_\ell(\hat{\mathbf{r}})$ (red arrows), also in a hot spot frame. Differences between $\mathbf{V}_\ell(\hat{\mathbf{r}})$ and $\mathbf{V}_m(\hat{\mathbf{r}})$ yield the best-fit directions of $\pm\hat{\mathbf{V}}_s(\hat{\mathbf{r}})$ shown in Fig. 3C. The 95% confidence ellipses in $\mathbf{V}_m(\hat{\mathbf{r}})$ incorporate formal uncertainty from inversion of $\hat{\mathbf{V}}_s(\hat{\mathbf{r}})$ plus uncertainty in the hot spot frame (*36*). Mantle flow is approximately eastward at 5.5 ± 1.5 cm/year (1σ).

mantle flow, produced by deeper mantle density heterogeneity, is unrelated to the velocity of the plate above and has essentially no influence on its motion or internal deformation.

The last few decades have seen the development of two basically incompatible views of the plate-mantle system. The tectonophysical view assumes effective decoupling between the plate and a stationary mantle by a mechanically weak asthenosphere. The plates are essentially "self-driving" (*49*). In the mantle dynamics view, the plates are strongly coupled to a mantle flow field that is driven by sources of buoyancy in the mantle (*7, 8*). Our results suggest that both views are partly correct when applied to westernmost North America. We do observe plate-mantle decoupling beneath a part of the plate, but we also find a mantle flow field that is likely driven by deep mantle density heterogeneity. If this description is correct, then beneath the oceanic two-thirds of Earth, where a weak asthenosphere is most likely present, we may be completely surprised by the actual motions of the mantle. More important, however, the direct measurement of these motions, as done here, holds the possibility of vastly increasing our understanding of the dynamic mantle.

References and Notes

1. R. M. Russo, P. G. Silver, *Science* **263**, 1105 (1994).
2. J. Polet *et al*., *J. Geophys. Res.* **105**, 6287 (2000).
3. V. Peyton *et al*., *Geophys. Res. Lett.* **28**, 379 (2001).
4. G. P. Smith *et al*., *Science* **292**, 713 (2001).
5. C. G. Chase, *Geophys. J. R. Astron. Soc.* **56**, 1 (1979).
6. B. H. Hager, C. R. O'Connel, *J. Geophys. Res.* **86**, 4843 (1981).
7. Y. Ricard, M. Richards, C. Lithgow-Bertelloni, *J. Geophys. Res.* **98**, 21895 (1993).
8. C. Lithgow-Bertelloni, M. A. Richards, *Rev. Geophys.* **36**, 27 (1998) and references therein.
9. S. van der Lee, G. Nolet, *Nature* **386**, 266 (1997).
10. ———, *J. Geophys. Res.* **102**, 22815 (1997).
11. S. P. Grand, D. V. Helmberger, *Geophys. J. R. Astron. Soc.* **76**, 399 (1984).
12. S. P. Grand, *J. Geophys. Res.* **99**, 11591 (1994).
13. Lithosphere consists of crust plus upper mantle and behaves in a plate-like manner over geologic time scales. Lithospheric shells, of thickness 70 to 200 km, move horizontally over the underlying mantle asthenosphere, which, in contrast, behaves more like a fluid. That the lithospheric mantle beneath westernmost North America is thin implies that uppermost mantle deformation is dominated by large horizontal shear strains.
14. P. G. Silver, *Annu. Rev. Earth Planet. Sci.* **24**, 385 (1996).
15. We assume that the surface and base-of-lithosphere velocities are the same (thin viscous sheet approximation) and that the orientation of shear is constant as a function of depth within the asthenosphere.
16. Although the spatial variation of $\mathbf{V}_m(\hat{\mathbf{r}})$ may be complicated in general, we assume the simplest possible mantle horizontal velocity field described by a rigid-body rotation.
17. S. Zhang, S. I. Karato, *Nature* **375**, 774 (1995).
18. Assuming that $\hat{\mathbf{V}}_s(\hat{\mathbf{r}})$ is known from shear-wave splitting, $\mathbf{V}_t(\hat{\mathbf{r}})$ is known from geodesy or other means, and ω_p is known, then it is possible to solve Eq. 1 for ω_m by nonlinear least squares, inverting for the components of ω_m that optimally align $\hat{\mathbf{V}}_\phi(\hat{\mathbf{r}})$ with $\hat{\mathbf{V}}_s(\hat{\mathbf{r}})$ for all points (*50*). For such an inversion, it is important that observations of ϕ cover a substantial portion of the plate boundary zone where significant differences in $\mathbf{V}_t(\hat{\mathbf{r}})$ occur.
19. East of the red areas, however, where the lithosphere is thicker, our assumption is unlikely to apply, as much of the anisotropy may lie within the lithospheric portion of the mantle (*14, 51*).
20. J. Polet, H. Kanamori, *Geophys. J. Int.,* in press.
21. D. L. Schutt, personal communication.
22. A. J. Haines, W. E. Holt, *J. Geophys. Res.* **98**, 12057 (1993).
23. W. E. Holt, A. J. Haines, *J. Geophys. Res.* **100**, 17991 (1995).
24. R. A. Bennett, J. L. Davis, B. P. Wernicke, *Geology* **27**, 371 (1999).
25. W. Thatcher *et al*., *Science* **283**, 1714 (1999).
26. C. Ma, J. W. Ryan, *NASA Space Geodesy Program—GSFC Data Analysis—1998, VLBI Geodetic Results 1979–1998* (NASA, Greenbelt, MD, 1998).
27. Southern California Earthquake Data Center (SCEC) (www.scecdc.scec.org:3128/group_e/release.v2).
28. U.S. Geological Survey (USGS) Earthquake Hazards Program (http://quake.wr.usgs.gov/QUAKES/geodetic/gps).
29. International GPS Service (IGS) GPS time series data (http://sideshow.jpl.nasa.gov/mbh/series.html).
30. J. T. Freymueller, M. H. Murray, P. Segall, D. Castillo, *J. Geophys. Res.* **104**, 7419 (1999).
31. R. McCaffrey *et al*., *Geophys. Res. Lett.* **27**, 3117 (2000).
32. T. H. Dixon *et al*., *Tectonics* **19**, 1 (2000).
33. K. Antonelis, D. J. Johnson, M. M. Miller, R. Palmer, *Geology* **27**, 299 (1999).
34. B. Shen-Tu, W. E. Holt, A. J. Haines, *J. Geophys. Res.* **104**, 28927 (1999).
35. L. M. Flesch, W. E. Holt, A. J. Haines, T. B. Shen, *Science* **287**, 834 (2000).
36. A. E. Gripp, R. G. Gordon, *Geophys. Res. Lett.* **17**, 1109 (1990).
37. To determine the covariance matrix for the rotation vectors, we calculate uncertainties in the rotation vectors assuming an uncertainty in ϕ of $\pm 10°$ and then perform Monte Carlo simulations for about 10,000 inversions, assuming Gaussian noise in the splitting observations. Errors in the model velocities $\mathbf{V}_t(\hat{\mathbf{r}})$ contribute no more than $\pm 2°$ in uncertainty in the direction of $\hat{\mathbf{V}}_\phi(\hat{\mathbf{r}})$ and hence were ignored in the calculation of the covariance matrix for the rotation vectors.
38. For supplemental data, see *Science* Online (www.sciencemag.org/cgi/content/full/295/5557/1054/DC1).
39. The statistical significance of the rotation value of ω_m in a hot spot frame can be determined using the χ^2 random value $\Psi = \mathbf{d}^\mathbf{T}\mathbf{V}^{-1}\mathbf{d}$, where $\mathbf{d}$ is the difference vector between the mantle frame we solved for and the hot spot frame (*36*), $\mathbf{V}^{-1}$ is the inverse of the covariance matrix for $\mathbf{d}$, and $\mathbf{T}$ denotes transpose. The 95% value for Ψ with three degrees of freedom (e.g., the value with a 5% chance of being exceeded if there is no real difference between our best-fit frame and the hot spot frame) is 7.8 (*52*). We calculate a value for Ψ of 28.0, which means that the calculated motion of the mantle in the hot spot frame is significantly different from zero at greater than the 99.9% confidence level. The reduced χ^2 value, χ^2_ν, of the angular misfits diminishes from 2.95 for the hot spot model (Fig. 3B) to 2.1 for the best-fit case (Fig. 3C), with three added degrees of freedom (total degrees of freedom = 216). An *F* test (*52*) shows that there is less than a 0.1% chance that the improved fit in Fig. 3C can be explained by random noise in the splitting observations. Therefore, the best-fit model in Fig. 3C is the preferred model.
40. This result is consistent with the sense of shear inferred from *P*-wave delays (*53*).
41. E. D. Humphreys, B. H. Hager, *J. Geophys. Res.* **95**, 19747 (1990).
42. In this case $\hat{\mathbf{V}}_s(\hat{\mathbf{r}})$ would be parallel to $\mathbf{V}_t(\hat{\mathbf{r}})$, the velocity field with respect to North America, which is clearly not the case [see (*24–35*)].
43. B. Steinberger, R. J. O'Connell, in *The History and Dynamics of Global Plate Motions,* M. A. Richards, R. G. Gordon, R. D. van der Hilst, Eds. (American Geophysical Union, Washington, DC, 2000), pp. 377–398.
44. C. Lithgow-Bertelloni, T. Becker, personal communication.
45. R. M. Richardson, L. M. Reding, *J. Geophys. Res.* **96**, 12201 (1991).
46. E. D. Humphreys, D. Coblentz, D. Schutt, *Eos* **81**, 13 (2000).
47. M. L. Zoback, M. D. Zoback, *Eos* **81**, 12 (2000).
48. As an illustration, for a Newtonian viscosity, for an asthenospheric thickness of 200 km, and assuming that the basal shear stress should be much less than 0.4 MPa (*35*) to have negligible cumulative effect on surface deformation across the region of interest, then the asthenospheric viscosity should be much less than 4×10^{19} Pa·s. Indeed, estimates of viscosity from post-seismic relaxation studies as well as Holocene shoreline rebound suggest upper mantle viscosities on the order of 10^{18} Pa·s (*54–58*).
49. R. M. Richardson, *J. Geophys. Res.* **97**, 11739 (1992).
50. For progressive simple shear, strain rates are expected to be of order 10^{-14} s^{-1} within the shearing layer, which yields a finite strain of unity in about 4 million years. Although $\hat{\mathbf{V}}_s(\hat{\mathbf{r}})$ reflects these finite displacements (finite strain) over the past several million years, Pacific–North America plate motion has remained relatively steady since 8 million years ago (Ma) (*59*) and became concentrated in the Gulf of California at about 5 Ma (*60*). Therefore, we infer that the surface velocity field (*24–35*) represents a steady-state feature that likely approximates lithospheric motion over the past 5 million years, and hence the directions of $\hat{\mathbf{V}}_s(\hat{\mathbf{r}})$ can be used to infer the instantaneous differential velocity between the surface and base of the asthenosphere using Eq. 1.
51. D. L. Schutt, E. D. Humphreys, *Geology* **29**, 291 (2001).
52. P. R. Bevington, *Data Reduction and Error Analysis for Physical Sciences* (McGraw-Hill, New York, 1969).
53. G. Bokelmann, *Geophys. J. Int.* **148**, 1 (2002).
54. J. S. Deng, M. Gurnis, H. Kanamori, E. Hauksson, *Science* **282**, 1689 (1998).
55. F. F. Pollitz, G. Peltzer, R. Burgmann, *J. Geophys. Res.* **105**, 8035 (2000).
56. A. M. Freed, J. Lin, *Nature* **411**, 180 (2001).
57. B. G. Bills, D. R. Currey, G. A. Marshall, *J. Geophys. Res.* **99**, 22059 (1994).
58. K. D. Adams, S. G. Wesnousky, B. G. Bills, *GSA Bull.* **111**, 1739 (1999).
59. T. Atwater, J. Stock, *Int. Geol. Rev.* **40**, 375 (1998).
60. M. Oskin, J. Stock, A. Martin-Barajas, *Geology* **29**, 459 (2001).

61. We thank P. Olson, D. Berkovici, S. Solomon, E. Humphreys, D. Schutt, C. Lithgow-Bertelloni, T. Becker, T. Atwater, C. Kreemer, and L. Flesch for helpful discussions; L. Flesch and B. Shen-Tu for help in setting up the kinematic model; and C. Kreemer for help in drafting the supplementary figure. This research has made use of GPS, very long baseline interferometry, and electronic distance measurement velocity data from numerous studies and agencies (*24–33*), including SCEC, USGS, and IGS, and we thank these groups for making such data available. We also thank J. Polet for making her manuscript available before publication, J. Dunlap for assistance with manuscript preparation, and S. Keiser for computer support. Figures were produced using GMT version 3.0 by P. Wessel and W. F. Smith. Supported by NSF grant EAR-0001160 (W.E.H.) and the Carnegie Institution of Washington.

5 October 2001; accepted 7 January 2002